

# Towards Computational Flapping Wing Aerodynamics of Realistic Configurations using Spectral Difference Method

Kui Ou\* and Antony Jameson †

*Aeronautics and Astronautics Department, Stanford University, Stanford, CA 94305*

In this paper high-order high-fidelity simulations of unsteady flows over flapping wings are examined. The numerical framework for the present computational flapping wings analysis is based on the high-order spectral difference (SD) scheme and a mesh deformation algorithms. The resulting method is capable of performing accurate and efficient simulations for unsteady flows over unsteady moving surfaces. This is demonstrated through several numerical experiments with increasing complexity in geometries and flow physics. The problems being studied include three-dimensional flows over an Eppler61 airfoil over a range of angles of attack at transitional Reynolds number of 46,000, and flows over an oscillating NACA0012 airfoil at Reynolds number of 40,000. In both cases three-dimensional simulations of the two-dimensional airfoils have been carried out. The numerical solver is finally applied to perform a three-dimensional flapping wing simulation of flows over a semi-complex wing-body configuration.

## I. Introduction

The concept of flapping wing based aerial vehicle has been the subject of intensive research in recent years. While our understanding of fixed wing aerodynamics has been vastly advanced in the past one hundred years, leading to efficient and high performance aircrafts of many kinds, no viable design of flapping wing based aerial vehicle emerges. Despite substantial research effort, flapping wing aerodynamics remains a difficult and challenging subject. The optimal aerodynamic performance of a flapping wing depends on many parameters, which include the wing planform shape, the cross-sectional airfoil shape, the material properties of the wing, the active and passive control of the flapping frequency, amplitude, and phase, as well as the complex combination of the various types of flapping motions such as plunging, pitching, twisting, and flexing. Such a large design space is best addressed with advanced optimization techniques. However, before this is feasible a good flow solver to accurately compute the flow field needs to be developed. High fidelity simulation of flow over a flapping wing is also very challenging in itself. The main difficulties include, firstly, resolving the unsteady three-dimensional vortex dominated flow; secondly, predicting the transition from laminar to turbulent flows at transitional Reynolds numbers; thirdly, modeling the fluid-structure coupling of the flow and the elastic wing surface. As a result, there are only very few existing numerical investigations of the complex three-dimensional unsteady viscous flows past a flapping wing.

Recent developments of advanced numerical algorithms and computational power, however, are beginning to make these challenges tractable. Modern high order methods, such as the Discontinuous Galerkin (DG) method, Spectral Difference (SD) method, and Flux Reconstruction (FR) method, have very small numerical dissipation, compared to traditional low order methods. They are well suited for resolving the vorticity structures in heavily vortex dominated flows. They are also unstructured flow solvers that allow complex geometries to be modeled. Furthermore, results from recent studies<sup>1-6</sup> indicate the potential benefit of relying on the inherent numerical dissipation of the high order schemes to act as a kind of subgrid scaled model, known as implicit LES (ILES). This means it might be possible for certain transitional flows to be directly simulated using the high order methods without the need of developing explicit LES models. Finally,

---

\*PhD Candidate, Aeronautics and Astronautics Department, Stanford University, AIAA Student Member.

†Thomas V Jones Professor, Aeronautics and Astronautics Department, Stanford University, AIAA Fellow.

aeroelastic solvers that combine high order Navier-Stokes solvers with finite element methods have received increasingly greater attention recently. Frameworks for accommodating dynamic mesh and fluid-structure coupling have been recently developed for various high order schemes.<sup>7-12</sup> These together make high-order method a competitive tool for numerical simulations of flapping wing aerodynamics. In the present work, high fidelity simulations of unsteady flows past a wing-body configuration were performed.

## II. Problem Setup

The geometry of the wing-body configuration is shown in Figure 1 (a) -(c) in three different views. The geometries of both the body and the wing are described by the equation for ellipsoid as in equation (1).

$$\frac{x^2}{a^2} + \frac{y^2}{b^2} + \frac{z^2}{c^2} = 1 \quad (1)$$

The center body is of the type of a prolate spheroid, while the wing has an elliptical planform with elliptical cross-sectional shape. The thickness to chord ratio of the cross-section is 0.15. The wing is positioned at the center of the body at mid height. The wing half span, measured from the tip to the edge of the body, is 6. The chord length at root is 1.

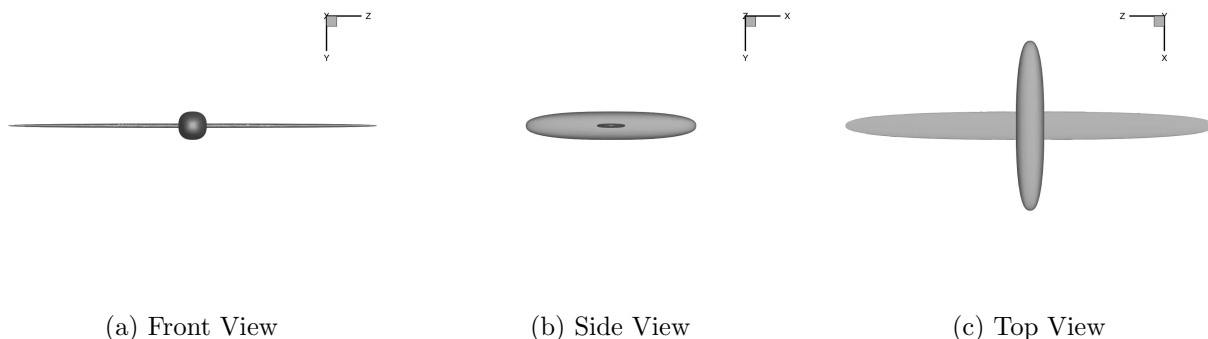


Figure 1. 3D view of the geometry for the wing-body configuration

The computational grid is generated using the meshing software from GridPro, and later converted into unstructured hexahedral elements. The surface mesh is shown in Figure 2 (a). A zoom of the mesh near the wing is shown in Figure 2 (b). A cross-section of the entire mesh domain is shown in (c). The mesh consists of 324,800 elements.

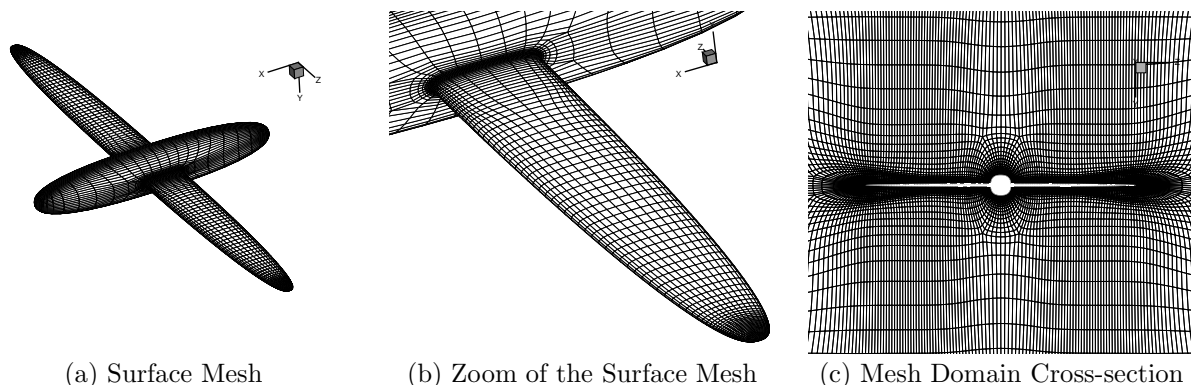


Figure 2. Mesh for the wing-body configuration

### III. Numerical Method

#### III.A. Unfiltered 3D Navier-Stokes Equations

The computations presented in this work are performed by the newly developed flow solver *SD3D*, a high-order accurate, unstructured, parallel solver for the Navier-Stokes equations. The *SD3D* code solves the unsteady, three-dimensional, compressible, unfiltered Navier-Stokes equations using the Spectral Difference method. The three-dimensional unfiltered Navier-Stokes equations can be expressed as follows:

$$\frac{\partial Q}{\partial t} + \frac{\partial F_I}{\partial x} + \frac{\partial G_I}{\partial y} + \frac{\partial H_I}{\partial z} = \frac{\partial F_V}{\partial x} + \frac{\partial G_V}{\partial y} + \frac{\partial H_V}{\partial z}. \quad (2)$$

where the state vector  $Q$ , inviscid flux vectors  $F_I, G_I$  and  $H_I$ , along with the viscous flux vectors  $F_V, G_V$  and  $H_V$ . Note that the equations presented above are the unfiltered Navier-Stokes equations and are used without change in different flow regimes (laminar, transitional and turbulent). No additional sub-grid stress and heat flux terms are added; the unresolved small eddies are accounted for by means of numerical dissipation.

#### III.B. 3D Spatial Discretization with Spectral Difference Method

In the present work, the Navier-Stokes equations are solved using the high-order Spectral Difference method for spatial discretization. The formulation of the equations on hexahedral grids is similar to the formulation of Liu et al.,<sup>14</sup> which will be summarized below for completeness.

Consider the unsteady compressible Navier-Stokes equations in conservative form written as:

$$\frac{\partial Q}{\partial t} + \frac{\partial F}{\partial x} + \frac{\partial G}{\partial y} + \frac{\partial H}{\partial z} = 0 \quad (3)$$

where  $F = F_I - F_V$ ,  $G = G_I - G_V$  and  $H = H_I - H_V$ . To achieve an efficient implementation, all element in the physical domain  $(x, y, z)$  are transformed into a standard cubic element,  $0 \leq \xi \leq 1, 0 \leq \eta \leq 1, 0 \leq \zeta \leq 1$ . The transformation can be written as

$$\begin{pmatrix} x \\ y \\ z \end{pmatrix} = \sum_{i=1}^K M_i(\xi, \eta, \zeta) \begin{pmatrix} x_i \\ y_i \\ z_i \end{pmatrix} \quad (4)$$

where  $K$  is the number of points used to define the physical elements,  $(x_i, y_i, z_i)$  are the Cartesian coordinates at those points, and  $M_i(\xi, \eta, \zeta)$  are the shape functions. The metrics and Jacobian of the transformation can be computed for the standard element. The governing equations in the physical domain are then transferred into the computational domain, and the transformed equations take the following form:

$$\frac{\partial \tilde{Q}}{\partial t} + \frac{\partial \tilde{F}}{\partial \xi} + \frac{\partial \tilde{G}}{\partial \eta} + \frac{\partial \tilde{H}}{\partial \zeta} = 0 \quad (5)$$

where  $\tilde{Q} = |J|Q$  and

$$\begin{pmatrix} \tilde{F} \\ \tilde{G} \\ \tilde{H} \end{pmatrix} = |J| \begin{pmatrix} \xi_x & \xi_y & \xi_z \\ \eta_x & \eta_y & \eta_z \\ \zeta_x & \zeta_y & \zeta_z \end{pmatrix} \begin{pmatrix} F \\ G \\ H \end{pmatrix} \quad (6)$$

The Jacobian matrix  $J$  is given by

$$J = \frac{\partial(x, y, z)}{\partial(\xi, \eta, \zeta)} = \begin{pmatrix} x_\xi & x_\eta & x_\zeta \\ y_\xi & y_\eta & y_\zeta \\ z_\xi & z_\eta & z_\zeta \end{pmatrix} \quad (7)$$

In the standard element, two sets of points are defined, namely the solution points and the flux points, as illustrated in Figure 3 for a 2D element. In order to construct a degree  $(N-1)$  polynomial in each coordinate direction, solution at  $N$  points are required. The solution points in 1D are chosen to be the Gauss points defined by:

$$X_s = \frac{1}{2} \left[ 1 - \cos \left( \frac{2s-1}{2N} \pi \right) \right], s = 1, 2, \dots, N. \quad (8)$$

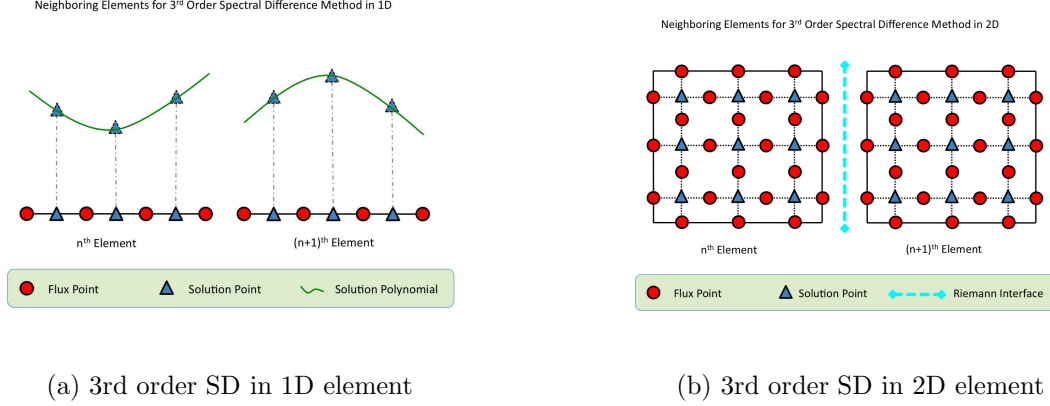


Figure 3. Position of solution (triangles) and flux (circles) points on the standard 1D (left) and 2D (right) element for 3rd order SD

The flux points were selected to be the Legendre-Gauss quadrature points plus the two end points 0 and 1, as suggested by Huynh.<sup>15</sup> Choosing  $P_{-1}(\xi) = 0$  and  $P_0(\xi) = 1$ , the higher-degree Legendre polynomials are

$$P_n(\xi) = \frac{2n-1}{n}(2\xi-1)P_{n-1}(\xi) - \frac{n-1}{n}P_{n-2}(\xi) \quad (9)$$

The locations of these Legendre-Gauss quadrature points are the roots of equations  $P_n(\xi) = 0$ . They are generally found to be more stable than the Gauss-Lobatto flux points and produce more accurate solutions for high-order spectral difference schemes. Using the solutions at  $N$  solution points, a degree  $(N-1)$  polynomial can be built using the following Lagrange basis defined as:

$$h_i(X) = \prod_{s=1, s \neq i}^N \left( \frac{X - X_s}{X_i - X_s} \right) \quad (10)$$

Similarly, using the fluxes at  $(N+1)$  flux points, a degree  $N$  polynomial can be built for the flux using a similar Lagrange basis as:

$$l_{i+1/2}(X) = \prod_{s=0, s \neq i}^N \left( \frac{X - X_{s+1/2}}{X_{i+1/2} - X_{s+1/2}} \right) \quad (11)$$

The reconstructed solution for the conserved variables in the standard element is the tensor product of the three one-dimensional polynomials,

$$Q(\xi, \eta, \zeta) = \sum_{k=1}^N \sum_{j=1}^N \sum_{i=1}^N \frac{\tilde{Q}_{i,j}}{|J_{i,j}|} h_i(\xi) h_j(\eta) h_k(\zeta) \quad (12)$$

Similarly, the reconstructed flux polynomials take the following form:

$$\begin{aligned} \tilde{F}(\xi, \eta, \zeta) &= \sum_{k=1}^N \sum_{j=1}^N \sum_{i=0}^N \tilde{F}_{i+1/2,j,k} \cdot l_{i+1/2}(\xi) \cdot h_j(\eta) \cdot h_k(\zeta) \\ \tilde{G}(\xi, \eta, \zeta) &= \sum_{k=1}^N \sum_{j=0}^N \sum_{i=1}^N \tilde{G}_{i,j+1/2,k} \cdot h_i(\xi) \cdot l_{j+1/2}(\eta) \cdot h_k(\zeta) \\ \tilde{H}(\xi, \eta, \zeta) &= \sum_{k=0}^N \sum_{j=1}^N \sum_{i=1}^N \tilde{H}_{i,j,k+1/2} \cdot h_i(\xi) \cdot h_j(\eta) \cdot l_{k+1/2}(\zeta) \end{aligned} \quad (13)$$

The reconstructed fluxes are only element-wise continuous, but discontinuous across cell interfaces. For the inviscid flux, a Riemann solver is employed to compute a common flux at interfaces to ensure conservation

and stability. In our case, we have used both the Rusanov solver<sup>13</sup> and the Roe solver to compute the interface inviscid fluxes. The viscous flux is a function of both the conserved variables and their gradients. Therefore, the solution gradients have to be calculated at the flux points. In our solver, the average approach described in reference<sup>14</sup> is used to compute the viscous fluxes.

#### IV. Mesh Deformation

Define the displaced mesh by  $(x, y, z)^{d.m}$ , the original undisplaced mesh by  $(x^r, y^r, z^r)$ , the translation displacement by  $(x^t, y^t, z^t)$ , the rotational angle by  $\theta$ , and the center of mesh rotation by  $(x_0^r, y_0^r, z_0^r)$ , the transformation from the stationary reference mesh to the rigidly translated and rotated mesh in  $x - y$  plane can now be represented as

$$\begin{bmatrix} x^{d.m} \\ y^{d.m} \\ z^{d.m} \end{bmatrix} = \begin{bmatrix} x^r \\ y^r \\ z^r \end{bmatrix} + \begin{bmatrix} x^t \\ y^t \\ z^t \end{bmatrix} + \begin{bmatrix} +\cos\theta & +\sin\theta & 0 \\ -\sin\theta & +\cos\theta & 0 \\ +0 & +0 & 1 \end{bmatrix} \begin{bmatrix} x^r - x_0^r \\ y^r - y_0^r \\ z^r - z_0^r \end{bmatrix} \quad (14)$$

Far away from the moving boundary, the flow domain is fixed and unchanged, and setting it as  $(x, y, z)^{f.m}$ , so that

$$\begin{bmatrix} x^{f.m} \\ y^{f.m} \\ z^{f.m} \end{bmatrix} = \begin{bmatrix} x^r \\ y^r \\ z^r \end{bmatrix} \quad (15)$$

In the region between the rigidly displaced mesh and the fixed stationary mesh, a polynomial blending function is constructed to provide smooth propagation for the unsteadiness in the mesh from one end to another. Polynomial with zero slope at the end points lead to orthogonality at the boundaries of the deforming region. In this study, a 5<sup>th</sup> order bending polynomial, as used by Persson et al,<sup>7</sup> is used. The form of the polynomial is:

$$bf = 10s^3 - 15s^4 + 6s^5 \quad (16)$$

where  $s = d/D$  is the ratio of the arc-length distance,  $d$ , of a point to the inner edge of the deforming region to the total width,  $D$ , of the deforming region. The rigidly displaced mesh can then be combined with the fixed stationary mesh through the deforming mesh using the blending polynomial to form the transformed mesh in the unsteady physical domain as:

$$\begin{bmatrix} x^p \\ y^p \\ z^p \end{bmatrix} = bf \begin{bmatrix} x^{f.m} \\ y^{f.m} \\ z^{f.m} \end{bmatrix} + (1 - bf) \begin{bmatrix} x^{d.m} \\ y^{d.m} \\ z^{d.m} \end{bmatrix} \quad (17)$$

For an elastic boundary under an externally applied load, the deformation distribution of the boundary can be obtained by solving the structure model. The computed deformation distribution allows us to displace the mesh from one grid point on the boundary to the next, and blend them to the farfield fixed mesh. However, in general the displacement distribution of an elastic boundary has non-vanishing slopes at its two ends, leading to unsmooth transition to its neighbouring mesh. To avoid this, a cubic spline function can be created by sampling the displacements along the elastic boundary and adding a point a small distance forward of the boundary and a second point a small distance aft of the boundary. By specifying zero derivative at those two additional points, the resultant cubic spline will have smooth transition to the surrounding undeformed mesh. Consider a general deforming elastic boundary in  $y$  direction, and take the straight line joining the two ends of the boundary as the reference x-axis, the coordinates of the deformed mesh can be represented as:

$$\begin{bmatrix} x^{d.m} \\ y^{d.m} \\ z^{d.m} \end{bmatrix} = \begin{bmatrix} x^r \\ y^r \\ z^r \end{bmatrix} + \begin{bmatrix} 0 \\ y_c^d(x^r) \\ 0 \end{bmatrix} \quad (18)$$

where  $y_c^d$  is the cubic spline function of the deformation distribution, including the two additional end points for smooth transition.

Once the boundary displacement at every grid point is known and the new mesh coordinates computed as above, the same blending technique used in the previous section can be implemented to smooth the vertical

displacement at the boundary to its far field stationary reference mesh. The coordinates of the entire mesh in the deformed physical space can now be written as:

$$\begin{bmatrix} x^p \\ y^p \\ z^p \end{bmatrix} = f_b \begin{bmatrix} x^r \\ y^r \\ z^r \end{bmatrix} + (1 - f_b) \begin{bmatrix} x^{d.m} \\ y^{d.m} \\ z^{d.m} \end{bmatrix} \quad (19)$$

Lastly, if the straight line joining the two ends of the boundary, which we treat as the reference x-axis, does not coincide with the real x-axis, then additional rotation and translation operations as outlined in the previous section should be carried out.

## V. SD Formulation on Dynamic Mesh

In order to formulate SD on a deforming mesh, we first consider the fact that a moving mesh at any new time instance leads to a new coordinate system. Hence one way to formulate the conservation laws with SD on deformable mesh is to implement unsteady coordinate transformation. The time-dependent transformation allows the boundary disturbance to propagate through the flow domain without deteriorating the accuracy of the spatial discretization method. Let's consider the unsteady coordinate transformation between the physical space in  $(x, y, z)$  and the reference space in  $(X, Y, Z)$ .

$$(X, Y, Z) = \mathbf{T}\mathbf{u}(x, y, z, t) \quad (20)$$

and we have:

$$X = X(x, y, z, t), \quad Y = Y(x, y, z, t), \quad Z = Z(x, y, z, t)$$

Again using the chain rule to arrive at the unsteady transformation gradient as:

$$\mathbf{G}_{\mathbf{T}\mathbf{u}} = \begin{bmatrix} \frac{\partial x}{\partial X} & \frac{\partial y}{\partial X} & \frac{\partial z}{\partial X} \\ \frac{\partial x}{\partial Y} & \frac{\partial y}{\partial Y} & \frac{\partial z}{\partial Y} \\ \frac{\partial x}{\partial Z} & \frac{\partial y}{\partial Z} & \frac{\partial z}{\partial Z} \end{bmatrix} \quad (21)$$

The Jacobian of the unsteady transformation gradient is equal to:

$$J_{T_u} = \det|G_{T_u}| \quad (22)$$

Using the chain rule for differentiation, and define the following new identities

$$\begin{aligned} \mathbf{U}^r &= J_{T_u} \mathbf{U}^p \\ \mathbf{F}^r &= J_{T_u} \left( \mathbf{F}^p \frac{\partial X}{\partial x} + \mathbf{G}^p \frac{\partial X}{\partial y} + \mathbf{H}^p \frac{\partial X}{\partial z} + \mathbf{U}^p \frac{\partial X}{\partial t} \right) \\ \mathbf{G}^r &= J_{T_u} \left( \mathbf{F}^p \frac{\partial Y}{\partial x} + \mathbf{G}^p \frac{\partial Y}{\partial y} + \mathbf{H}^p \frac{\partial Y}{\partial z} + \mathbf{U}^p \frac{\partial Y}{\partial t} \right) \\ \mathbf{H}^r &= J_{T_u} \left( \mathbf{F}^p \frac{\partial Z}{\partial x} + \mathbf{G}^p \frac{\partial Z}{\partial y} + \mathbf{H}^p \frac{\partial Z}{\partial z} + \mathbf{U}^p \frac{\partial Z}{\partial t} \right) \end{aligned} \quad (23)$$

where superscript  $p$  denotes variables in the physical domain, while superscript  $r$  denotes variables in the reference domain. The governing equation in the new reference coordinate space in the unsteady case still assumes the same conservation law form:

$$\frac{\partial \mathbf{U}^r}{\partial t} + \frac{\partial \mathbf{F}^r}{\partial X} + \frac{\partial \mathbf{G}^r}{\partial Y} + \frac{\partial \mathbf{H}^r}{\partial Z} = 0 \quad (24)$$

Note that the entire computation is carried out based on the reference domain. When physical space solution is needed, the computed reference space solution can be readily mapped using the mapping Jacobians.

## VI. Domain Decomposition and Parallelization

The spectral difference method is a highly efficient high-order accurate method that is well suited for large-scale time-dependent computations in which high accuracy is required. The discontinuous nature of the spectral difference scheme and the fact that the current implementation of the 3D spectral difference method uses an explicit time advancement scheme makes our current 3D code well suited for parallel computer platforms.

First, the domain is partitioned using the graph partitioning code METIS. Once the domain is decomposed, each processor updates the solution at the interior points of the cells in its domain following the same procedure as in the serial code. For element interfaces that are adjacent to a partition boundary, non-blocking sends and receives are used to exchange the right and left state vector  $Q^L$  and  $Q^R$ , along with the gradient of the state vectors  $\nabla Q^R$  and  $\nabla Q^L$ , so that the procedure to compute the flux values at the interface can be applied. The MPI-based parallelization of the code is thus highly efficient due to the non-blocking strategy used.

## VII. Numerical Validations

In contrast to problems with fixed surface conditions, flows over dynamic moving boundaries tend to be much more complex and usually exhibit those following characteristics:

- flows experience high local and instantaneous angles of attack
- flows tend to be heavily vortex-dominated
- flows experience local high Reynolds number
- flows tend to transit very readily from laminar to turbulent

These flows are very unsteady and complex. Experiments for these flows can be very difficult to perform accurately. Accurate data collections can also be very hard. Numerical validation of flow solvers for this type of problem also proves very challenging. Nevertheless, validation efforts have been attempted to address some of the challenging aspects of flapping wing aerodynamics. More specifically, high angle of attack flows are investigated by considering flows over an Eppler61 airfoil. Flows over moving boundaries are studied for the case of a plunging-pitching Naca12 airfoil. In both cases, 3D simulations of the airfoils have been performed to allow for the spanwise variation of the flows.

### VII.A. 3D Simulation of Flows over an Eppler61 Airfoil

Careful experimental studies have been carried out by Burns<sup>21</sup> for flows over the Eppler61 airfoil over a range of angles of attack and Reynolds numbers. In this paper, investigation of three-dimensional simulation of flow over the Eppler61 airfoil at a transitional Reynolds number of 46,000 has been conducted. The flow is solved with 5th order spectral difference method on a 96x16x16 mesh. We have investigated the flow over the Eppler61 airfoil at a range of angle of attacks. The angle of attacks studied include 6°, 8°, 10°, 12°, and 14°.

We compare the lift and drag coefficients with both wind tunnel and water tunnel experimental data.<sup>20</sup> The numerical results can fairly accurately predict the angle of stall and the drag rise point, as shown in Figure 5. The present results tend to overpredict the lift, but this overprediction is not unique in our case. Our computational results quite closely match the numerical results (not plotted here) by Mittal 2010.<sup>6</sup> However, note that the variation between the computational results and experimental results are well within the variation between the experiments themselves.

The flow patterns of the various cases are visualized by plotting the Mach and vorticity contours, and the vorticity isosurfaces, as shown in Figure 4 and Figure 6. For the flow condition with Mach=0.2 and Re=46,000, the 5th order SD solution seems to be able to capture the transition from laminar to turbulent flow, and resolve the small scale turbulent feature of flow separation. This is illustrated by the vorticity isosurface plots. The 3D results obtained so far have been quite promising. Work is ongoing to qualitatively predict the separation, transition and reattachment locations and to compare them with the experimental data (see Burns 1981<sup>21</sup>).

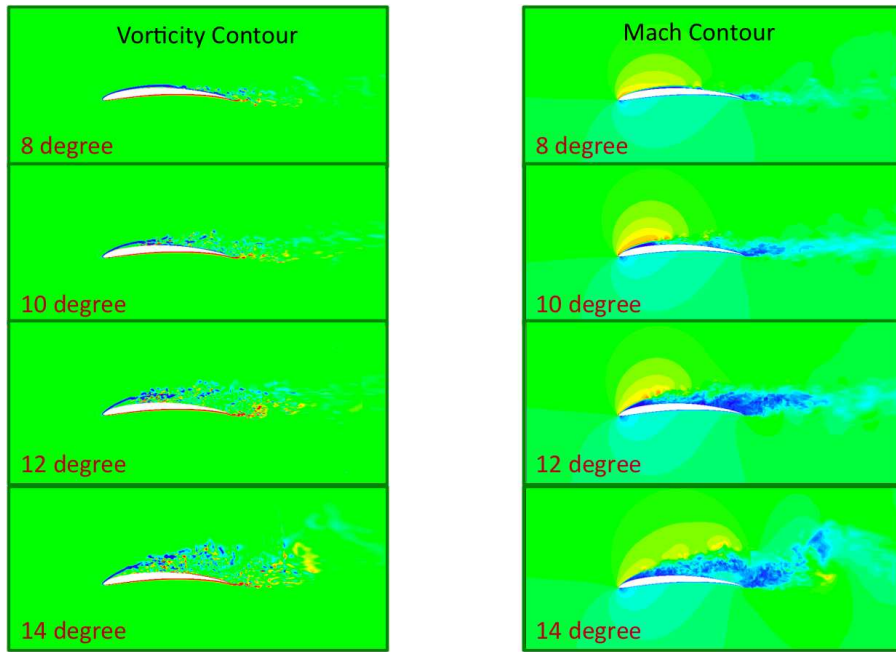


Figure 4. Vorticity and Mach contours at mid-span for flows over the Eppler61 airfoil at increasing angles of attack.

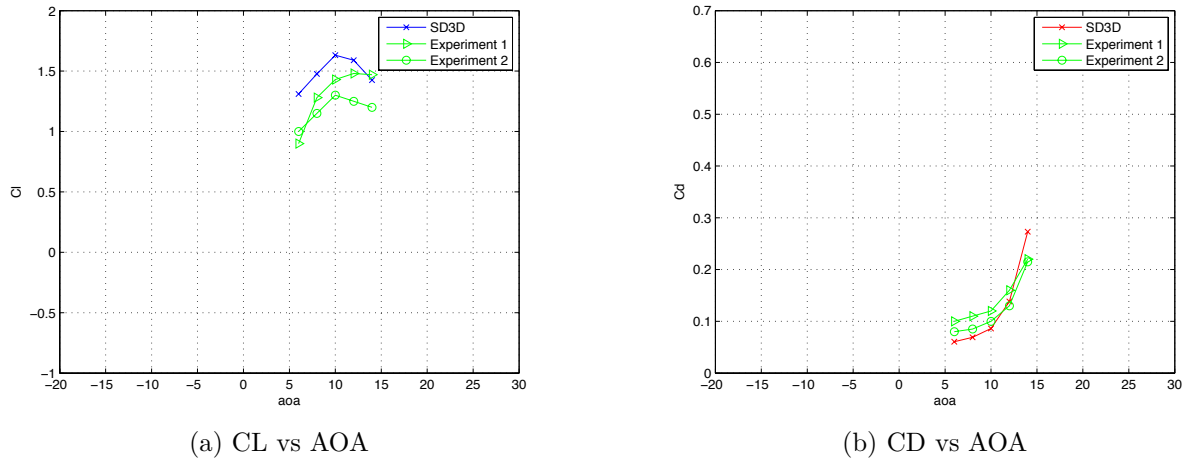


Figure 5. Comparison of CL and CD curves between SD3D and experiments. Experiment 1 is the water tunnel result. Experiment 2 is the wind tunnel result.

### VII.B. 3D Simulation of the Flow over a Plunging-Pitching NACA12 Airfoil

As an effort to validate the current numerical scheme for solving problems involving dynamic boundary movements, unsteady flows, vortex shedding and, potentially, transitional behavior, simulation of the flow over an oscillating NACA12 airfoil has been performed. The simulation is based on the experimental work by Triantafyllou etc.<sup>17</sup> Experiments were conducted on a NACA0012 airfoil at Reynolds number 40,000. Force and power data were measured. In particular an optimum propulsive performance of the oscillating airfoil was obtained. The optimal production of thrust occurred for a phase angle between plunge and pitch motion of  $\psi = 75^\circ$ , pitching axis around the one-third chord, plunging amplitude of  $h_0 = 0.75c$ , and maximum angle of attack  $\alpha_0 = 15^\circ$ . These are the parameters used for the present simulation.

The mesh used is very similar to the one used for the Eppler61 airfoil case, with an initial size of  $96 \times 16 \times 16$ . Fourth order SD solutions have been calculated. The resulting temporal variations of the CL and CD curves are plotted in Figure 7. A sequence of plots of the vorticity isosurface at different time instances is plotted in Figure 8. From these plots, the presence of many small-scaled turbulent like flow

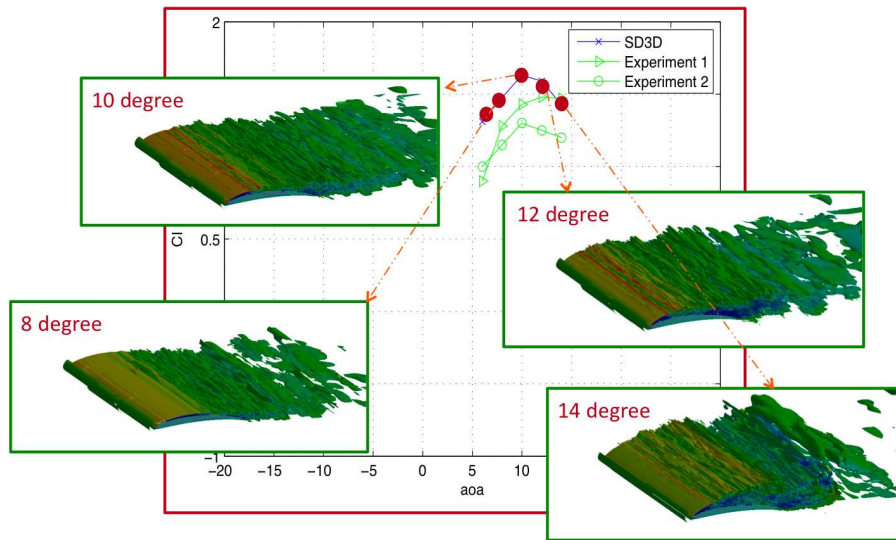


Figure 6. Overlay of the vorticity isosurface plots with  $C_L - \alpha$  curve. The isosurfaces are colored by the magnitude of the local Mach number.

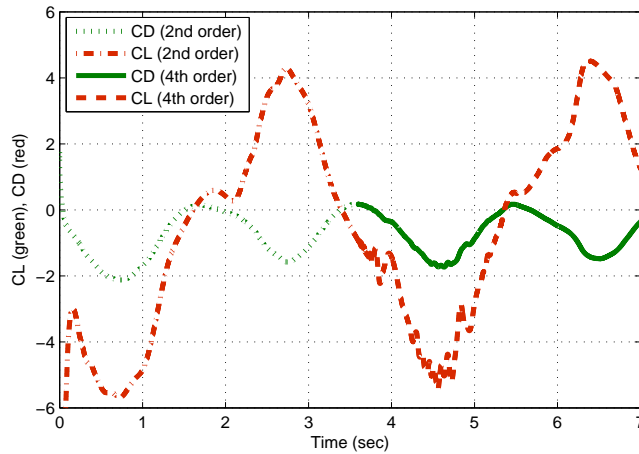


Figure 7. Temporal variations of the lift and drag coefficients. The red lines are the CL curves. The green lines are the CD curves. The curves comprise of both second and fourth order solutions. The dash-dot line is 2nd order CL curve; the dotted line is the second order CD curve; the dash line is the 4th order CL curve; the solid line is the 4th order CD curve.

structures can be clearly observed. These small-scaled structures coexist with some larger-scaled laminar bubbles.

The pressure, vorticity and Mach contour plots at mid-span of the airfoil are shown in Figure 9 at various time instances. The negative sign of the  $C_D$  curve indicates the production of thrust. The time averaged thrust coefficients  $C_T$  have been computed for different Strouhal numbers, while holding other parameters unchanged. The resulting  $C_T$  vs Strouhal number curves are plotted in Figure 10 (a) for various cases. In this plot, two dimensional solutions have been computed using the SD method, up to the 4th order, for Strouhal numbers of 0.1, 0.2, 0.3, 0.4 and 0.5. The resulting curve follows the trend predicted by the experiment, but under-predicts the thrust. An estimate of the results from other CFD efforts shows a similar behavior, i.e. they follow the trend but under-predict the magnitude of thrust. Their results, however, are closer to the experiment than the second order SD results. Details of these other CFD results are shown in Figure 10 (b), excerpted from the Shyy et al.<sup>18</sup> The discrepancy between the SD2D result and the experiment result could be attributed to 3D effect. Indeed, the current 3D simulations of the Naca0012 airfoil show a dramatic improvement of the thrust prediction. Due to the high computational cost associated with 3D high-order simulations, only two Strouhal number cases have been computed. Nevertheless, the agreement of the existing results with the experiment is quite good.

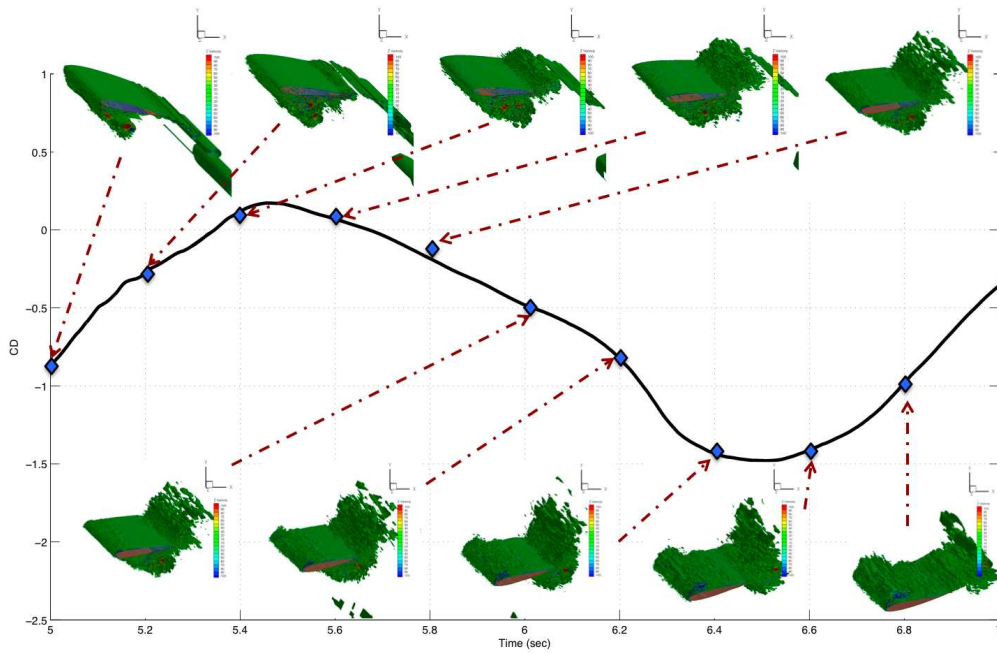


Figure 8. Temporal evolution of the vorticity isosurface is plotted against the CD curve.

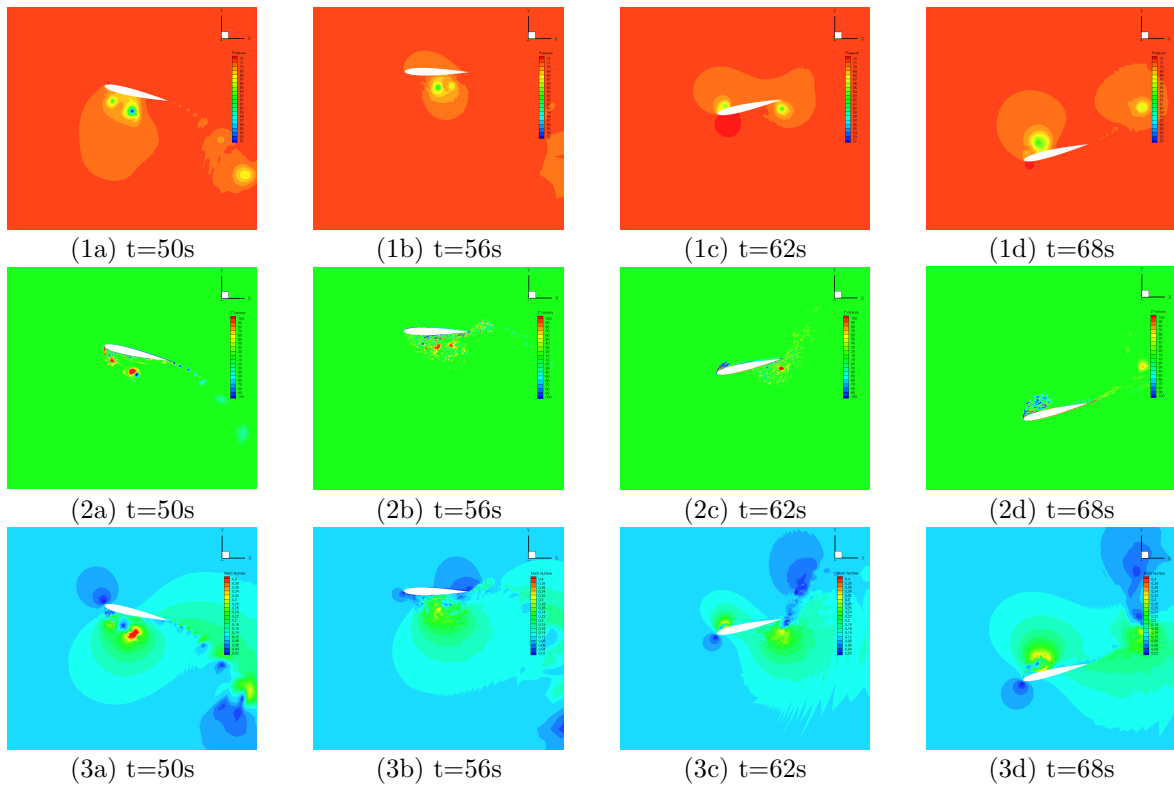


Figure 9. Details of the flow fields at mid-span at various time instances. Top row figures display the pressure contours. Middle row shows the vorticity contours. Bottom row shows the Mach contours.

## VIII. Flapping Wing Results

### VIII.A. Effect of Wing Flapping on Forward Thrust

With many conceivable flapping wing kinematics, it will be useful to quickly explore the effectiveness of some of these flapping motions in terms of lift and thrust generation. In this section, a series of simulations

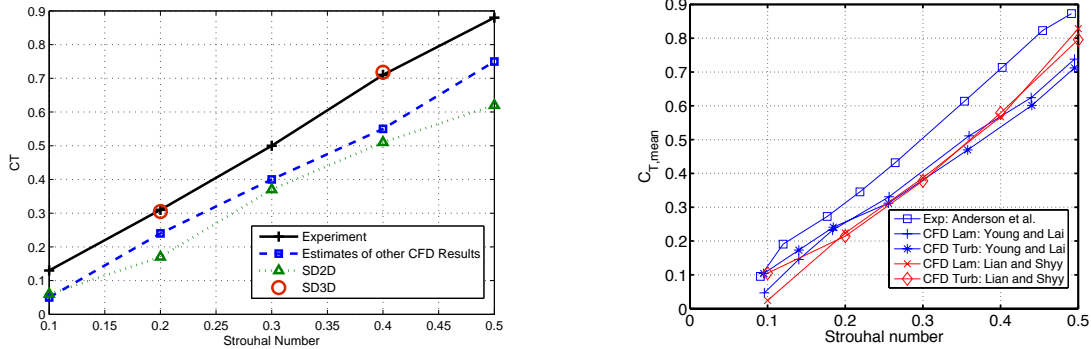
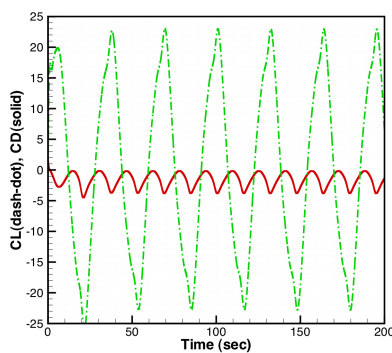
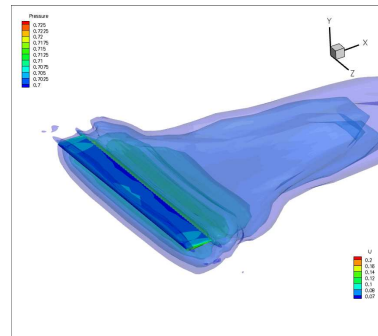


Figure 10. Comparisons of plots of thrust coefficient versus Strouhal number. Left figure compares the experimental data with the simulation results from the present study. Right figure is a reference plot summarizing the results from other simulation efforts.<sup>18, 19</sup>

were carried out to study just this. To reduce the demand for computational resources, consider a pair of Naca0012 wing without the center fuselage. The 3D mesh has 20,458 hexahedral elements. The following results were obtained using  $2^{nd}$  order SD method, since the goal of the present section is to get a feel for the effect of flapping motion on lift and thrust, not the details of the flow fields. The flapping wing studies here cover the pure plunging motion, a combined pitching and twisting motion, and a sinusoidal deforming motion. The flow conditions are Mach=0.05 and Re=2,000. The Strouhal numbers, based on the amplitude at the wing tip, for all cases are St=0.3. The lift and thrust results, together with the streamwise momentum deficit contours, are summarized in Figure(11) for the plunging motion, Figure(12) for the combined pitch and twisting motion, and Figure(13) for the deforming motion.



(a) Lift and Thrust coefficients



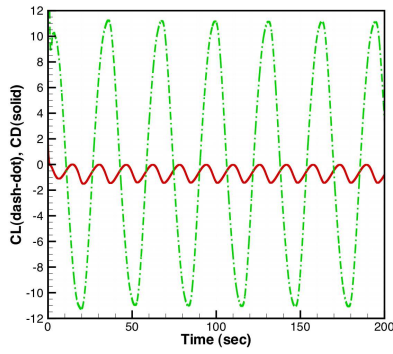
(b) streamwise momentum deficit contours

Figure 11. Aerodynamic force coefficients time history and streamwise momentum deficit contours for a plunging Naca0012 wing at M=0.05 and Re=2000

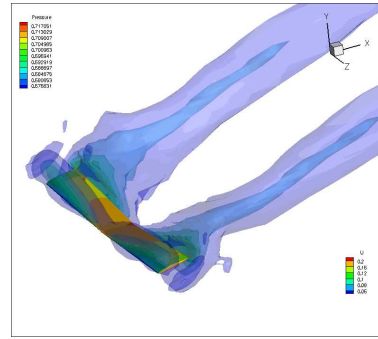
In those plots, the streamwise momentum deficit contours have been generated. By doing so, it is easy to observe that the flow velocities behind the flapping wing have been increased relative to the freestream value. By increasing the momentum of fluid passing through the wing, in close analogy to the mechanism of propellers, the flapping motion has resulted in thrust production. The Figures here are presented in the order of decreasing level of forward thrust. As can be observed from the momentum deficit contour plots, the magnitude of thrust is directly related to the total amount of fluid behind the wing that has greater-than-freestream velocities.

### VIII.B. Flows over a Wing-Fuselage Flapping Wing Configuration

In this section, a semi-complex wing-fuselage geometry is considered, as an effort towards more realistic flapping wing simulations. The details of the geometry and mesh were discussed earlier in section II. In the simulation, we considered a low Reynolds number, low Mach number flow over the wing-fuselage configura-

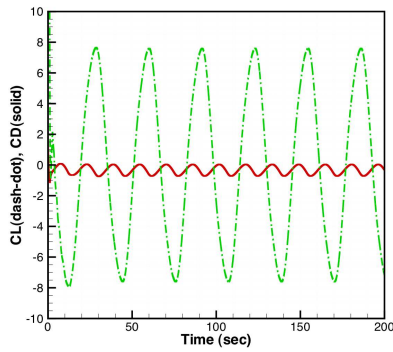


(a) Lift and Thrust coefficients

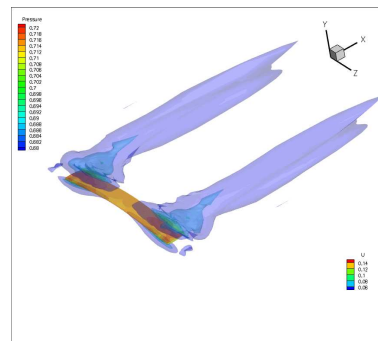


(b) streamwise momentum deficit contours

Figure 12. Aerodynamic force coefficients time history and streamwise momentum deficit for a pitching-twisting Naca0012 wing at  $M=0.05$  and  $Re=2000$



(a) Lift and Thrust coefficients



(b) streamwise momentum deficit contours

Figure 13. Aerodynamic force coefficients time history and streamwise momentum deficit for a deforming Naca0012 wing at  $M=0.05$  and  $Re=2000$

tion. While the Reynolds number based on the freestream is low, the local velocities induced by the flapping motion can lead to three dimensional flows. Even at the chosen low Reynolds number of 5,000, the simulated flows based on the current mesh are most likely under-resolved. Fully resolving the flows for the full sized configuration demands more computing resource than is available to the present authors. Nevertheless, the following results demonstrate a more complete numerical framework for flapping wing simulations and some interesting results were obtained.

### VIII.B.1. Steady Flow at Zero Angle of Attack

Steady state solution of the flow was computed first. The converged solution was used as the initial condition for the subsequent flapping wing simulation. The flow conditions for the steady flow are  $Mach = 0.05$ ,  $Re = 5,000$  and  $\alpha = 0$ .

With an initial mesh of 324,800 cells, the flow is solved with 4<sup>th</sup> order SD method. The steady state results are shown in Figure(14). The pressure contour of the front cross section of the airplane shows a symmetrical pressure distribution along the top and bottom of the wing, as expected for an symmetrical uncambered wing profile. The presence of fuselage results in a pressure drop in the center. In Figure(14)(c), the streamwise velocity contour is plotted at the middle plane, showing the velocity distribution along the fuselage. Again, the flow is symmetrical between the top and bottom surfaces. Finally, the surface pressure contour is shown in Figure(14)(b). The converged drag coefficient based on the wing surface area is  $CD_{total} = 0.13$ .

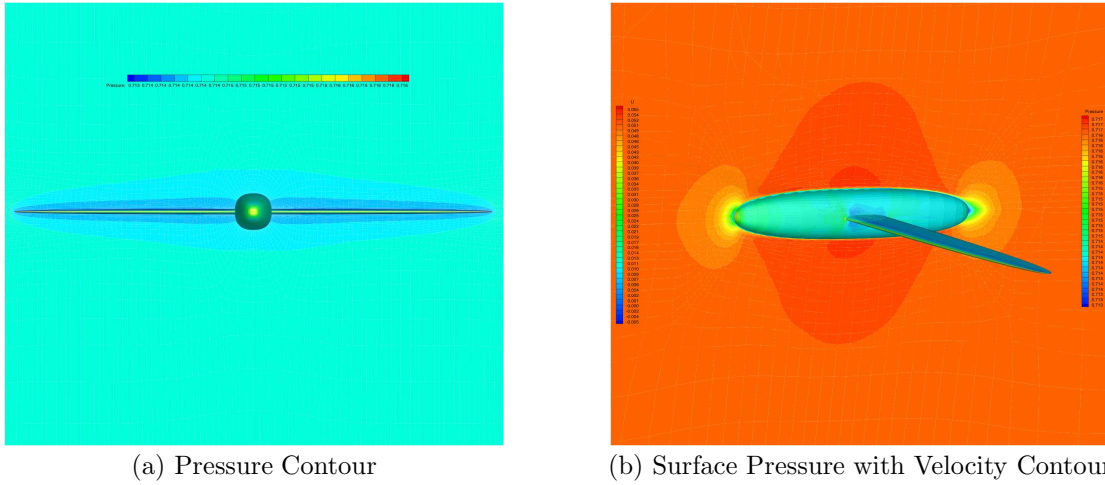


Figure 14. Pressure and velocity contours of steady state flow over the airplane at  $M=0.05$  and  $Re=5000$

### VIII.B.2. Flapping Flight at Zero Angle of Attack with Sinusoidal Motion

For flapping wing simulation, the wing-fuselage configuration is flapping with a sinusoidal motion. The amplitude along the span follows a harmonic variation. The resulting rate of change of the amplitude is a sinusoidal function.

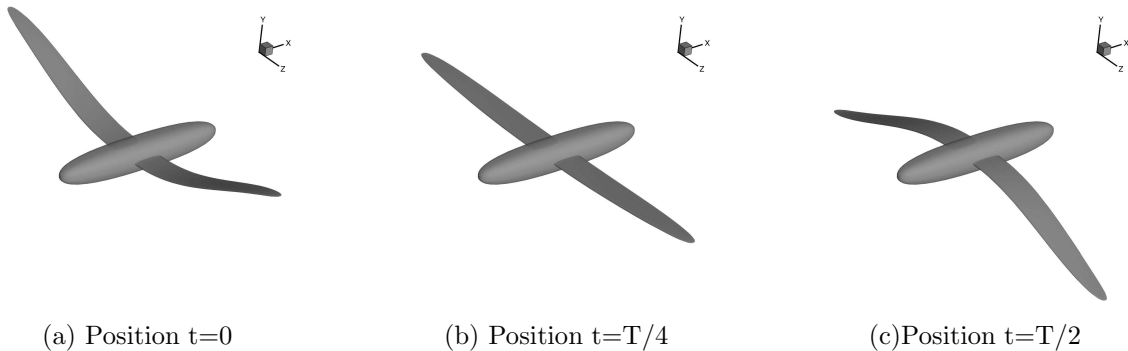


Figure 15. Symmetrical flapping wing motion at (a) maximum, (b) zero, and (c) minimum flapping amplitude.  $T$  is the period of flapping motion.

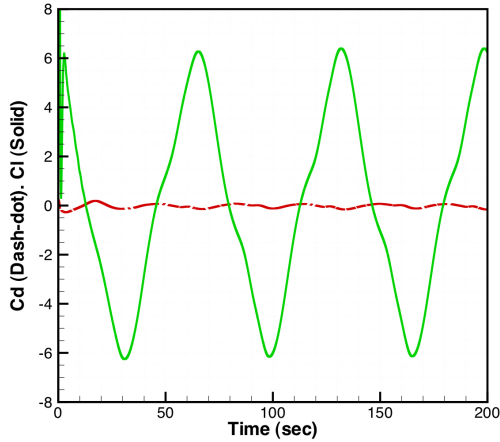
The spatial and temporal variation of the motion are expressed as

$$y = A \sin\left(2\pi \frac{z}{L}\right) \sin(2\pi ft)$$

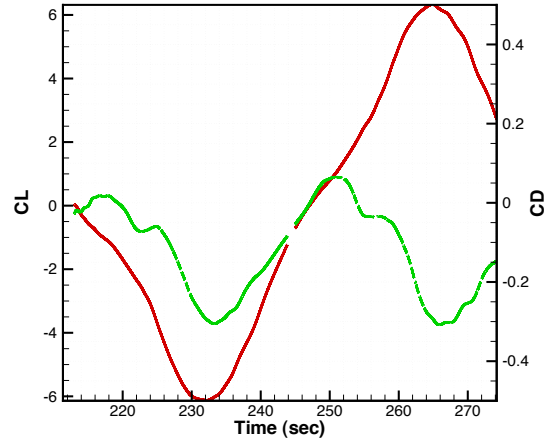
where  $A$  is the maximum amplitude at the wing tip,  $L$  determines the flapping spatial distribution, and  $f$  is the frequency of the flapping motion. We have used the following values:  $A = 1$ ;  $L = 15$ ;  $f = 0.015$ . This corresponds to a Strouhal number of 0.3. Strouhal number between 0.2 and 0.3 is generally considered good for flapping flight, since many natural flyers fly in this similar reduced frequency regimes. Choosing the optimal flapping parameters is beyond the scope of the present study. The parameters are selected based on studies discussed in the previous section.

The flapping wing simulations were performed until converged periodical flow solution were obtained. The temporal variations of the lift and drag coefficients are presented in Figure (16). On average, no lift is produced, but a forward thrust is generated through the flapping motion, as indicated by the negative value of the drag coefficient.

To correlate the details of the flow field with the force coefficients, the entropy isosurfaces are plotted in Figure 17 together with the  $CL$  and  $CD$  values at the corresponding time instances. From the plots it can be observed that flows are highly unsteady near the wing tips where surface movements are greatest. At the fuselage and inboard portion of the wings, the flows remain fairly laminar and steady, as indicated by the absence of flow entropy.



(a) CL and CD temporal variations



(b) Zoom of the CL(solid red) and CD (green dash) plots

Figure 16. Time histories of CL and CD for the flow over the flapping wing-fuselage configuration at  $M=0.05$ ,  $Re=5000$  and  $Str=0.3$

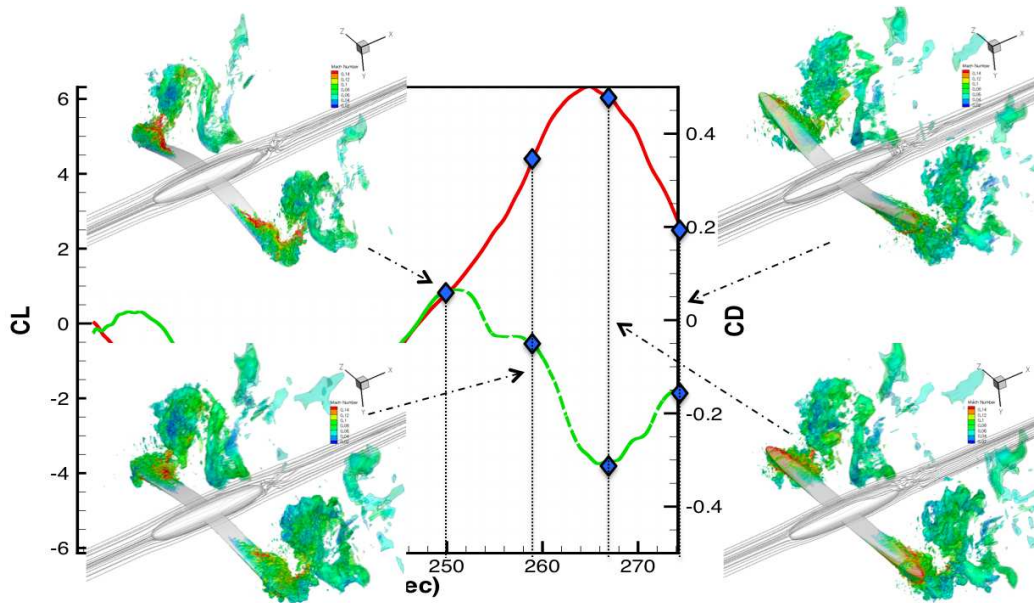


Figure 17. Entropy isosurface at various time instances, plotted against the CL and CD curves. The entropy isosurface is colored by the magnitude of the Mach number.

Figure 18 plots the surface pressure contour and the pressure contour of the flow field at one-third span location at various time instances, while Figure 19 plots in addition the entropy isosurfaces, where the color on the isosurface indicates the magnitude of the local Mach number.

The formation of the vortical tube along the wing leading edge at  $t = 250s$  can be clearly seen from Figure 19 (a). This happens near the end of a wing stroke. The low pressure region of the vortex core can be correlated with the pressure contour plot in Figure 18 (a). The maximum lift position, for example at  $t=267$ , also corresponds to the largest pressure differential between the wing upper and lower surface, as clearly shown in Figure 18 (c). This is the instance when the wing reaches its peak flapping velocity.

The drag curve of Figure 16(b) indicates the presence of a double-peak profile in each flapping cycle. By relating the quantitative isosurface plots with the qualitative flow contours, it can be observed that each double-peak occurs at the end of each flapping cycle. At this phase of the cycle, the wing reverses its flapping direction. Many vortices, large or small, are formed. During this short instance, i.e. shortly

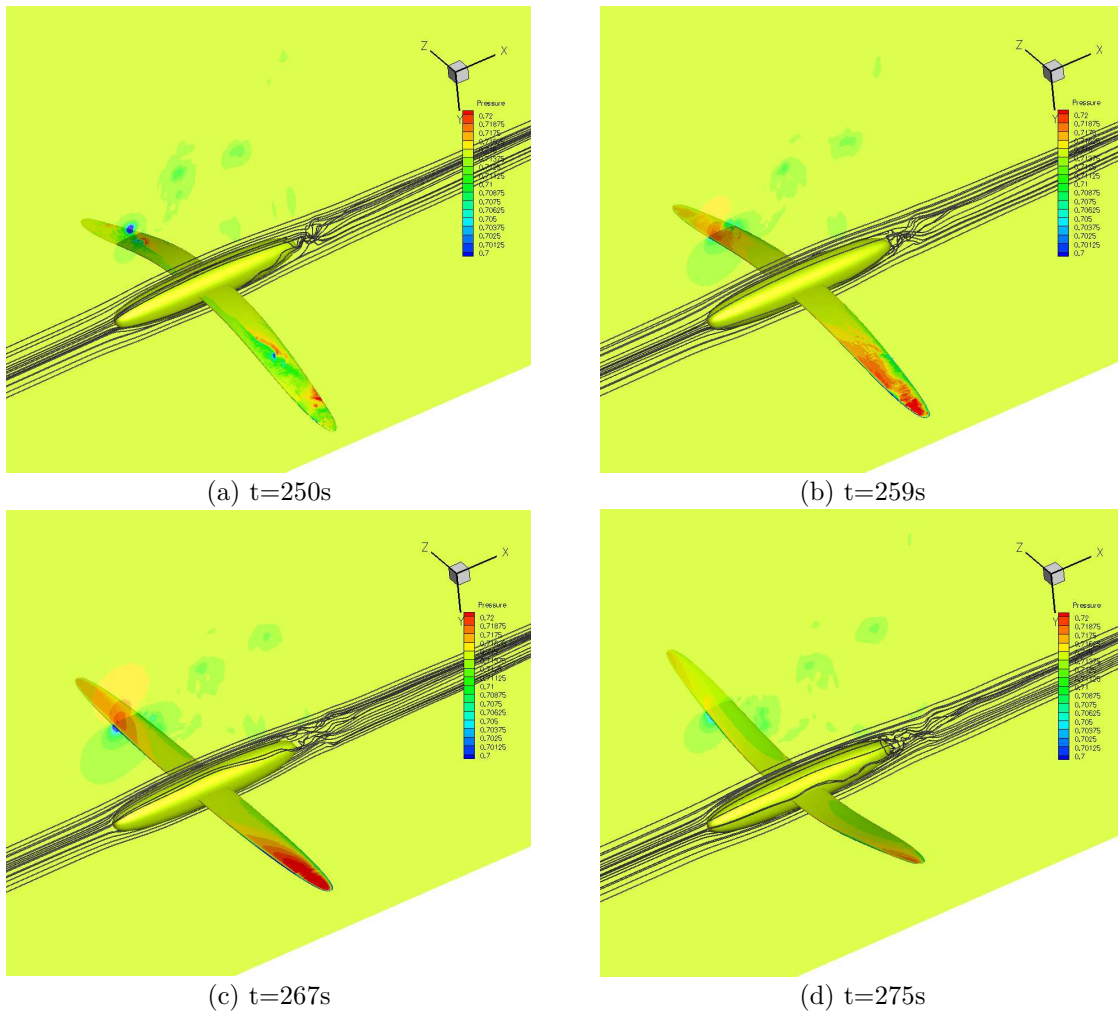


Figure 18. Surface pressure contour of the wing-fuselage configuration and the pressure contour of the flow field at one-third span location at various time instances.

after the breakdown of the old vortices at the bottom surface and before the formation of the new leading edge vortices at the upper surface, the flows are stagnant and chaotic as the old leading vortices travel downstream and interact with the reverse moving trailing edge. This momentary stagnation of local flow speed lead to a loss of lift and increase of drag. This is evident in the entropy plot of Figure 19(b) which shows a chaotic breakdown of the vortices. The rough surface pressure contour of Figure 18(b) also indicates this phenomena. Further evidence can be found from the plunging-pitching Naca12 airfoil. In Figure 8, between roughly  $t=5.4$  and  $t=6.2$ , there is a upward bump in the drag coefficient curve (and correspondingly a downward shift of lift, as can be seen in Figure 7 in the same time span). The corresponds to a period when there is no strong leading edge vortex being formed while the old spanwise vortices interacting heavily with each other, especially near the trailing edge. This is probably the most chaotic and stagnant phase in each flapping wing cycle. The secondary peak in the lift and drag curve occurs during this phase of the flapping cycle.

## IX. Conclusion

In order to perform numerical simulations of flows over flapping wings, a numerical framework for accommodating boundary movements is a prerequisite. The mesh deformation method outlined in this work, based on a smooth algebraic blending of the surface boundary and the far field boundary, proves to be an efficient method for this purpose, occurring very little cost to the baseline flow solver. Formulating the mesh deformation in terms of a coordinate transformation also allows its very efficient integration into the

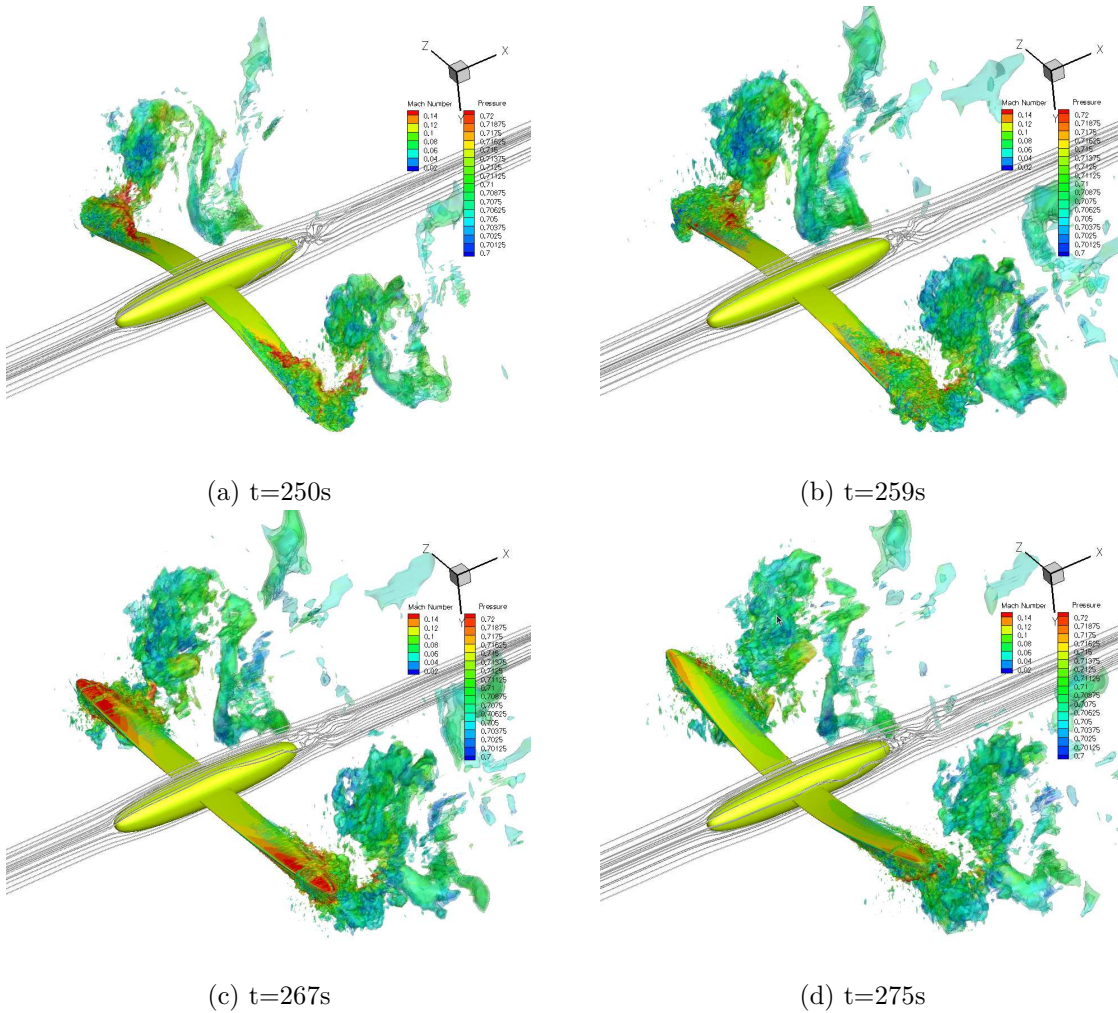


Figure 19. Surface pressure contour of the wing-fuselage configuration and the entropy isosurfaces, colored by the magnitude of Mach number, at various time instances.

unstructured high order SD scheme. Numerical simulations with increasing complexity have been performed. In the first case, the three-dimensional simulations of the 2D Eppler61 airfoil are used to validate the SD flow solver. For flows over a range of angles of attack, the current method is able to capture the trend of the experimental  $C_L - \alpha$  curve and predict the stall angle. In the second case, flows over a plunging-pitching NACA0012 airfoil are examined. Like the Eppler61 case, flows exhibit transitional behaviors. The thrust coefficients at various Strouhal numbers were computed and the agreements with experimental data are excellent. This particular flapping mode of this airfoil has been found to be very efficient in producing thrust. Simulations of flows over a 3D wing-body flapping wing configurations were finally performed. Numerically predicted force coefficients indicate that a symmetric flapping motion at a suitable Strouhal number leads to production of thrust. It is found that some interesting patterns in the temporal variations of the CL and CD curves can be correlated to and explained by the interaction of vortices by careful examination of the flow fields. In summary, these analyses act as essential building blocks towards the eventual goal of conducting complete flapping wing simulations of realistic configurations.

## X. Acknowledgements

This research has been made possible through the support of the Air Force Office of Scientific Research under grants FA9550-07-1-095 and FA9550-10-1-0418, and the National Science Foundation under grants 0708071 and 0915006. The authors would also like to thank Peter Eiseman of Program Development Company for providing the GridPro meshing software that is used for creating and gridding the wing-body

configuration.

## References

- <sup>1</sup>M. Galbraith and M. Visbal, *Implicit large eddy simulation of low Reynolds number flow past the SD7003 airfoil*, AIAA Paper 2008-225 (2008).
- <sup>2</sup>M. R. Visbal *High-Fidelity Simulation of Transitional Flows past a Plunging Airfoil*, AIAA Journal, Vol. 47, No. 11, November 2009
- <sup>3</sup>Uranga, A., P. Persson, M. Drela, and J. Peraire (2009). Implicit Large Eddy Simulation of Transitional Flows Over Airfoils and Wings. *AIAA P.*, vol. **4131**. 19th AIAA Computational Fluid Dynamics, San Antonio, Texas, June 22-25, 2009, 17 p.
- <sup>4</sup>P. Castonguay, C. Liang, and A. Jameson, *Simulation of transitional flow over airfoils using the spectral difference method*, AIAA Paper 2010-4626 (2010).
- <sup>5</sup>K. Ou, P. Castonguay and A. Jameson, *3D Flapping Wing Simulations with High Order Spectral Difference Method on Deformable Mesh*, 49th AIAA Aerospace Sciences Meeting, Orlando, Florida, January, 2011.
- <sup>6</sup>S. B. Savaliya, S. P. Kumar, and S. Mittal, *Laminar separation bubble on an Eppler 61 airfoil*, Int J Numer Meth Fl **64**, 627 (2010).
- <sup>7</sup>P.O.Persson, J.Peraire and J.Bonet, *Discontinuous Galerkin solution of the Navier-Stokes equations on deformable domains*, AIAA Conference, AIAA-2007-0513, Reno, NV, January 2007.
- <sup>8</sup>P.-O. Persson, J. Peraire, J. Bonet, "A High Order Discontinuous Galerkin Method for Fluid-Structure Interaction", 18th AIAA Computational Fluid Dynamics Conference, June 2007. AIAA-2007-4327
- <sup>9</sup>K. Ou and A. Jameson *A High- Order Spectral Difference Method for Fluid- Structure Interaction on Dynamic Deforming Meshes* , AIAA-2010-4932, 28th AIAA Applied Aerodynamics Conference, Chicago, Illinois, 28 Jun - 1 Jul 2010
- <sup>10</sup>K. Ou and A. Jameson *Flow Induced Cylinder Oscillation and Its Control with High Order Spectral Difference Method on Deformable Mesh* , ASME 2010 3rd Joint US-European Fluids Engineering Summer Meeting, Montreal, Quebec, Canada, 1 August - 5 August 2010
- <sup>11</sup>K. Ou and A. Jameson *On the Temporal and Spatial Accuracy of Spectral Difference Method on Moving Deformable Grids and the Effect of Geometric Conservation Law*, AIAA-2010-5032, 40th Fluid Dynamics Conference and Exhibit, Chicago, Illinois, 28 Jun - 1 Jul 2010
- <sup>12</sup>K. Ou, C. Liang, A. Jameson, "High-Order Spectral Difference Method for the Navier-Stokes Equations on Unstructured Moving Deformable Grids", AIAA-2010-541, 48th AIAA Aerospace Sciences Meeting, Orlando, Jan 2010.
- <sup>13</sup>V. V. Rusanov, *Calculation of interaction of non-steady shock waves with obstacles*, Journal of Computational Math Physics USSR, Vol. 1, pp.261-279, 1961.
- <sup>14</sup>Y. Liu, M. Vinokur, and Z. J. Wang, *High-Order Multidomain Spectral Difference Method for the Navier-Stokes Equations on Unstructured Hexahedral Grids*, Communications in Computational Physics **Vol 2**, Number 2, pp 310-333 (2006).
- <sup>15</sup>H. T. Huynh, *A flux reconstruction approach to high-order schemes including discontinuous Galerkin methods*, Number AIAA-2007-4079, AIAA Computational Fluid Dynamics Conference, 2007.
- <sup>16</sup>K. D. Jones and C. M. Dohring and M. F. Platzer, *Experimental and computational investigation of the Knoller-Betz effect* , AIAA Journal, vol 36, 780-783, 1998
- <sup>17</sup>Anderson, J.M., Streitlien, K., Barrett, D.S. and Triantafyllou, M.S. (1998) Oscillating foils of high propulsive efficiency, J. Fluid Mech., 360, pp. 41-72.
- <sup>18</sup>Y. Lian, and W. Shyy, "Aerodynamics of Low Reynolds Number Plunging Airfoil under Gusty Environment", AIAA 2007-71,45th AIAA Aerospace Sciences Meeting and Exhibit, 8 - 11 January 2007, Reno, Nevada
- <sup>19</sup>Lai, C.S.J. and Platzer, F.M. (1999) Jet Characteristics of a Plunging Airfoil, Aiaa J., 37(12).
- <sup>20</sup>Mueller, T., Kellogg, J., Ifju, P., Shkarayev, S., *Introduction to the Design of Fixed Wing Micro Air Vehicles.*, AIAA Education Series. AIAA, 2006.
- <sup>21</sup>Burns, T. F. *Experimental studies of the Eppler 61 and Pfenninger airfoils at low Reynolds numbers*. Masters Thesis, The University of Notre Dame, January 1981.